



Supplementary Materials for

Atomically thin two-dimensional organic-inorganic hybrid perovskites

Letian Dou, Andrew B. Wong, Yi Yu, Minliang Lai, Nikolay Kornienko, Samuel W. Eaton, Anthony Fu, Connor G. Bischak, Jie Ma, Tina Ding, Naomi S. Ginsberg, Lin-Wang Wang, A. Paul Alivisatos, Peidong Yang*

*Corresponding author. E-mail: p_yang@berkeley.edu

Published 25 September 2015, *Science* **349**, 1518 (2015)
DOI: 10.1126/science.aac7660

This PDF file includes:

Materials and Methods
Supplementary Text
Figs. S1 to S17
Tables S1 to S4

Materials and Methods

Synthesis of the 2D hybrid perovskites.

Reagents: Unless otherwise stated, all of the chemicals were purchased from Sigma-Aldrich Chemical and used as received.

Synthesis of $C_4H_9NH_3Br$: 10 mL of butylamine and 25 mL of methanol were added to a 250 mL round bottom flask. The mixture was stirred and maintained at 0 °C using an ice-water bath. 10 mL of HBr (50 wt% in water) was added to the mixture dropwise. The ice-water bath was removed and the mixture was stirred at room temperature for 2 hours. Then the solvent (methanol and water) was removed by a rotary evaporator at 70 °C. The crude oil-like material was washed with diethyl ether by stirring the solution for 30 min, a step which was repeated for three times, and finally recrystallized from a mixed solvent of diethyl ether and ethanol. After filtration, the white solid was collected and dried at 60 °C in a vacuum oven for 24 h. Another related chemical, CH_3NH_3Br , was purchased from 1-material Inc. and used without further purification.

Growth of $(C_4H_9NH_3)_2PbBr_4$ thin sheets: All the solution preparation and thin sheets growth were carried out inside an argon-filled glove box with oxygen and water level less than 1 ppm. The as-synthesized $C_4H_9NH_3Br$ (308 mg, 2 mmol) and $PbBr_2$ (367 mg, 1 mmol) were dissolved in 2 mL of anhydrous dimethylformide (DMF) inside a 4 mL vial. The solution was then diluted 100 times by a DMF/chlorobenzene (1:1 volume ratio) co-solvent. Before use, the diluted solution was further diluted 10 times by either chlorobenzene (CB) or CB/acetonitrile (2:1 volume ratio) co-solvent. Si/SiO₂ was used as the substrate for the 2D perovskite growth. Si/SiO₂ substrates were cleaned by ultrasonication in isopropanol, acetone, water, and isopropanol again for 5 min; then dried by a nitrogen gun. The substrates were then transferred into a glove box and preheated at 75 °C on a hot plate. 10 μL of the diluted solution was dropped onto the Si/SiO₂ surface and dried at 75 °C for 10 min. Thin sheets of $(C_4H_9NH_3)_2PbBr_4$ grew spontaneously as the solvent evaporated. All other chloride, iodide, and alloy derivatives were synthesized using a similar procedure.

Growth of $(C_4H_9NH_3)_2(CH_3NH_3)Pb_2Br_7$ thin sheets: All the steps were the same as above except for the solution preparation: $C_4H_9NH_3Br$ (154 mg, 1 mmol), CH_3NH_3Br (56 mg, 0.5 mmol) and $PbBr_2$ (367 mg, 1 mmol) were dissolved in 2 mL of anhydrous dimethylformide (DMF) inside a 4 mL vial.

Mechanical exfoliation of the $(C_4H_9NH_3)_2PbBr_4$ thin sheets: Single crystals of $(C_4H_9NH_3)_2PbBr_4$ were prepared by the slow cooling of the hot solution (90 °C) of $C_4H_9NH_3Br$ (308 mg, 2 mmol) and $PbBr_2$ (367 mg, 1 mmol) in 20 mL DMF/toluene mixture with 2 drops of HBr aqueous solution. The sheet-like crystals were then attached to a regular scotch tape and the part of the tape with the crystals was refolded upon a clean adhesive section of the same piece of tape; the two layers were then pressed firmly together for several seconds. The tape was gently unfolded so that two mirrored crystal areas on the tape remained. This process was repeated for 4-5 times. Then the Si/SiO₂

substrate was placed shiny-side down on area with the crystals and pressed firmly to the tape for several seconds. It was then gently removed, and the sample was washed in hexanes.

Solvent exfoliation of the $(C_4H_9NH_3)_2PbBr_4$ thin sheets: 1 mg of the $(C_4H_9NH_3)_2PbBr_4$ single crystal was added to 2 mL of anhydrous hexanes and the mixture was ultrasonicated for 10 min to fully exfoliate and disperse the material. The suspension was then diluted 10 times by hexanes. 10 μ L of the diluted solution was drop-casted on the Si/SiO₂ substrate and dried at 60 °C for 10 min.

Characterization of the 2D hybrid perovskites.

Optical microscopy (OM) measurements: OM images of the thin sheets were taken using a Zeiss Axio Scope.A1 in dark field mode. The 2D hybrid perovskites directly grown, drop-casted from hexane dispersion, and mechanically exfoliated on Si/SiO₂ substrate were used for the measurements.

Atomic force microscopy (AFM) measurements: AFM images of the thin sheets were taken using an Asylum MFP 3D in tapping mode. The 2D hybrid perovskites directly grown, drop-casted from hexane dispersion, and mechanically exfoliated on Si/SiO₂ substrate were used for the measurements.

X-ray diffraction (XRD) measurements: Powder X-ray diffraction was measured using a Bruker AXS D8 Advance diffractometer with a Cu K α source. Single crystal X-ray diffraction was measured using APEX II QUAZAR diffractometer with a Mo K α source, an APEX II detector. A colorless plate 0.040 x 0.040 x 0.020 mm in size was mounted on a Cryoloop with Paratone oil. Data were collected in a nitrogen gas stream at 100(2) K using phi and omega scans. Crystal-to-detector distance was 40 mm and exposure time was 10 seconds per frame using a scan width of 2.0°. Data collection was 100.0% complete to 25.000° in q. A total of 28141 reflections were collected covering the indices, $-9 \leq h \leq 9$, $-9 \leq k \leq 9$, $-33 \leq l \leq 33$. 1678 reflections were found to be symmetry independent, with a R_{int} of 0.0376. Indexing and unit cell refinement indicated a primitive, orthorhombic lattice. The space group was found to be P b c a (No. 61). The data were integrated using the Bruker SAINT software program and scaled using the SADABS software program. Solution by iterative methods (SHELXT) produced a complete heavy-atom phasing model consistent with the proposed structure. All non-hydrogen atoms were refined anisotropically by full-matrix least-squares (SHELXL-2014). All hydrogen atoms were placed using a riding model. Their positions were constrained relative to their parent atom using the appropriate HFIX command in SHELXL-2014.

Transmission electron microscopy (TEM) and energy dispersive spectroscopy (EDS) measurements: To grow the 2D sheets on TEM grids, lacy carbon TEM grids were put on the surface of a Si/SiO₂ substrate and a drop of the dilute solution was added and dried at 75 °C. All TEM images and SAED patterns were acquired using FEI TitanX 60-300 microscope operated at 60kV. Before taking SAED patterns, the camera was calibrated

using a standard copper film calibration sample. The electron diffraction simulation was performed using the MacTempas software (34). Structure models (Fig.1a, Fig.S8) were drawn using the VESTA software (35).

Grazing incidence wide angle X-ray scattering (GIWAXS): GIWAXS spectra were taken at beamline 7.3.3. at the Advanced Light Source (ALS) at Lawrence Berkeley National Lab utilizing an incident wavelength of 10 keV. 2D spectra were recorded with a Pilatus 2M-2D detector and integrated to reduce to 1D with NIKA GIWAXS software.

Steady state photoluminescence (PL) measurements: Photoluminescence measurements were performed using the 325 nm He:Cd laser. The full intensity of the beam is 5 mW. Using an iris diaphragm and a focusing lens, a Gaussian beam spot with a waist of approximately 30 μm was obtained and used to excite individual 2D sheets. The output power of the excitation source was adjusted by neutral density filters (normally 1 ~ 100 μW) and monitored with an external energy meter. Emission from 2D sheets was collected with a dark-field microscope objective (Nikon 50 \times , N.A. 0.55, in a Nikon ME600 optical microscope) and routed via a bundled optical fiber to a UV-vis spectroscopy spectrometer (Princeton Instruments/Acton) equipped with a 1200 groove/mm grating blazed at 300 nm and a liquid N₂-cooled charge-coupled device. During the measurement, the sample was placed in a vacuum chamber with a vacuum level of 2×10^{-3} torr. For the low temperature measurements, liquid helium was used to keep the sample at about 6 K and the vacuum was maintained at 2×10^{-6} torr to avoid moisture condensing on the sample. There was no obvious sample damage by laser during the measurement. Internal QE was calculated from the ratio of the integrated PL signal of a 2D sheet at 298K and 6K.

Time-resolved photoluminescence (TRPL) measurements: Time resolved photoluminescence was collected on a Picoquant Fluotime 300 with PMA 175 detector and an LDH-P-C-405 diode laser (excitation wavelength of 407.1 nm) at room temperature.

Raman spectroscopy: The Raman spectra were taken by a Horiba HR800 system with laser excitation wavelength of 780 nm. The laser is focused to a diameter of 2 mm and has a power of 300 mW. For the Raman measurement, 2D crystals were grown on Mica instead of Si/SiO₂ to avoid a strong background signal. The signals at 100 and 200 cm^{-1} are from the Mica substrate.

Cathodoluminescence measurements: Cathodoluminescence (CL) images were acquired with a modified Zeiss Gemini SUPRA 55 Scanning Electron Microscope (SEM). An aluminum parabolic reflector was positioned above the same sample in order to couple a 1.3π sr of emission outside of the vacuum chamber through a quartz window. Emission at 410 nm was collected using a H7360-01 photon counting head (Hamamatsu) with a 40 nm bandpass filter centered at 415 nm. All images were acquired at 3 kV with 512 x 512 pixels and a scanning rate of 10 ms/line.

Density functional theory (DFT) simulations: The calculations are based on density functional theory within the generalized gradient approximation (GGA) formulated by Perdew, Burke, and Ernzerhof (PBE) as implemented in VASP code. The projector augmented wave (PAW) pseudopotentials are employed, and the valence wavefunctions are expanded in a plane-wave basis with an energy cutoff of 400 eV. For the lattice constant calculations, the primitive cell is employed and the Brillouin zone integration is sampled with a $3 \times 3 \times 1$ k-point mesh. Larger energy cutoffs and finer k-point meshes have been tested, and the difference is negligible.

The calculated in-plane lattice constants are 8.27 and 8.46 Å for the single layer; 8.25 and 8.40 Å for the bulk crystal. The lattice constant of the bulk is in good agreement with the experimental values. The slight overestimation is well known in PBE functional calculations. The calculated lattice constant of the single layer is ~ 0.1 Å larger than that of the bulk, which is however, smaller than the experimental lattice expansion. Because we calculate isolated material and the substrate effect is not taken into account, the large lattice expansion in experiments may be induced by the substrate and needs further investigation. The calculated band gap for the bulk crystal is 2.59 eV (using experimental lattice constant data of the bulk sample), and the single layer sheet is 2.61 eV (using GIWAXS experimental lattice constant data of the few layer sample). These values are consistent with the experimental results.

Supplementary Text

Discussion of the synthetic conditions for the ultrathin 2D hybrid perovskite crystals. Many parameters affect the growth of the 2D sheets, and the parameter range is flexible within a certain degree. Under the optimized condition, the volume ratio of DMF, CB, and acetonitrile is around 1:13:6. We found that it is necessary to have 4% ~ 6% DMF to facilitate the dissolution of the precursors (because without DMF, the precursors cannot dissolve). Between 25% to 40% acetonitrile is required to achieve square-shaped 2D sheet formation. The growth temperature can be from 60 to 100 °C. Lower temperatures led to particles with random shape and higher temperatures damaged the 2D sheets and resulted in poor surface morphology. We varied the concentration of the precursors and found the 2D sheets form within a window of 0.02% ~ 0.04% of $(\text{C}_4\text{H}_9\text{NH}_3)_2\text{PbBr}_4$ by weight. Lower concentration gave only small dots and higher concentration gave large particles with random shapes. We also note that the 2D sheets can grow on different substrates such as Si/SiO₂, Si, quartz, Mica, aluminum foil, etc.

The role of acetonitrile: We noticed that if using a DMF/CB binary solvent, DMF is “too good” of a solvent and CB is “too bad” of a solvent for the hybrid perovskites, and the ratio of DMF to CB is hard to control to achieve effective crystallization during solvent evaporation. The purpose underlying the use of an intermediate solvent, such as acetonitrile, is to balance the dissolution and crystallization of the 2D hybrid perovskites. Acetonitrile has a higher vapor pressure and can leave the solution more quickly under heating, so the CB:DMF ratio increases and induces the crystal formation. Any further role of acetonitrile in the growth mechanism is still unclear. Further study is necessary to fully understand the mechanism.

We noticed that the thickness distribution is quite wide (from ~2 to ~50 nm) and the average thickness (number of layers) is dependent on growth temperature and solution concentration. Under the optimized condition (75 °C, 0.03%), the average thickness is ~10 nm. Higher concentration (75 °C, 0.04%) gave relatively thicker samples with an average of ~15 nm. We also found slightly higher or lower temperature all gave relatively thicker samples. Although we observe some initial trend, there was sample-to-sample variation, which is possibly because there may be more factors that need to be taken into account. A more detailed study has been carried out to fully understand the growth mechanism as well as to achieve more precise control of the lateral size and thickness of the 2D sheets.

Discussion on the PL of the ultrathin 2D hybrid perovskite crystals.

The blue shift of the PL is probably from the structural relaxation of the in-plane crystal lattice. Our TEM and GIWAXS measurements show a slight increase of the in-plane lattice constant for the few layer samples, as compared to the bulk crystal, and the lattice expansion should lead to a small increase of the band gap. To confirm this, we have carried out DFT simulations. The calculated band gap for the bulk crystal is 2.59 eV (using the measured bulk lattice constant), while the calculated band gap of a single layer sheet is 2.61 eV (using the measured few layer lattice constants from GIWAXS). The band gap increase of 20 meV is in good agreement with the experimental observation.

The reason that the PL of the 22-layer sample is more close to that of the 8-layer and 3-layer samples but far from the bulk is probably because the bulk crystal is much thicker (at least several micrometers, over 500 layers) than the 22-layer and 8-layer samples and possesses a slightly different lattice constant. As a result, the structure of the 22-layer sample is more close to the 8-layer and 3-layer samples (indeed the lattice constant calculated from TEM diffraction pattern for thinner and thicker (e.g. 22-layer) sheets are very similar, and they are different from the bulk value). There could be many reasons for that, e.g., some coherence or interaction with the substrate.

There are two possible effects that may contribute to the asymmetric peak shape of the PL emission. One contributing effect is the existence of the Γ_2^- and the Γ_1^- excitonic states in the energy range plotted. As proposed in ref. 26, these states emerge because of the splitting of the energy levels caused by the exchange interactions between the electron and hole within the layered perovskite. As shown in Fig. 3H, these states can be distinguished by PL at 6K with the Γ_1^- state being slightly red-shifted and less bright (the spin 1 dark exciton due to exchange interaction) relative to the Γ_2^- state, but these states cannot be clearly resolved at room temperature, which may contribute to the asymmetry of the PL peak. A second possible contributing effect stems from the coupling of the excitonic states to phonons, which has been proposed in related materials such as for $(\text{C}_6\text{H}_5\text{C}_2\text{H}_4\text{-NH}_3)_2\text{PbI}_4$ by Gauthron et al. (ref. 17) and for $(\text{C}_4\text{H}_9\text{NH}_3)_2(\text{PbI}_2)$ by Wu et al. (ref. 31). In both cases, the PL reported in these works showed a broad lower energy tail, which was attributed to these interactions. In the work by Wu et al., it was proposed that the exciton-phonon interactions lead to the formation of self-trapped excitons. In the case of PL broadening from self-trapping, the few layer 2D sheet would still be expected to exhibit this self-trapping behavior, as the deformation energy would remain low as the number of layers decreases. Therefore, we believe that it is likely that a 3-layer $(\text{C}_4\text{H}_9\text{NH}_3)_2\text{PbBr}_4$ sheet may experience this effect strongly, which may explain the asymmetric PL from the sample.

Supplementary figures

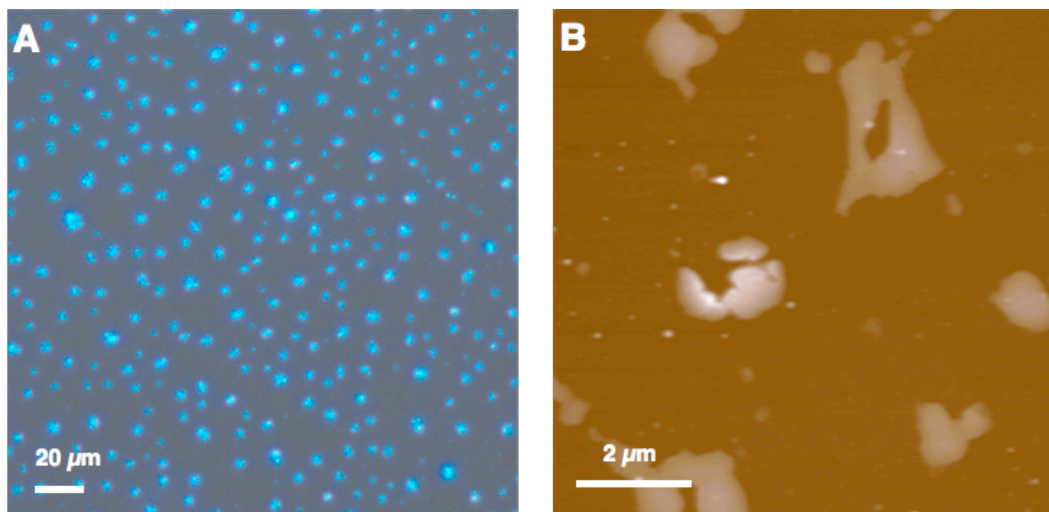


Fig. S1. Direct growth of thin $(\text{C}_4\text{H}_9\text{NH}_3)_2\text{PbBr}_4$ using dimethylformamide and chlorobenzene co-solvent. (A) Optical image. (B) AFM image. The crystallization and growth processes are not uniform, leading to random shape multi-layer sheets. Only tiny single layer particles with diameters smaller than 200 nm can be found.

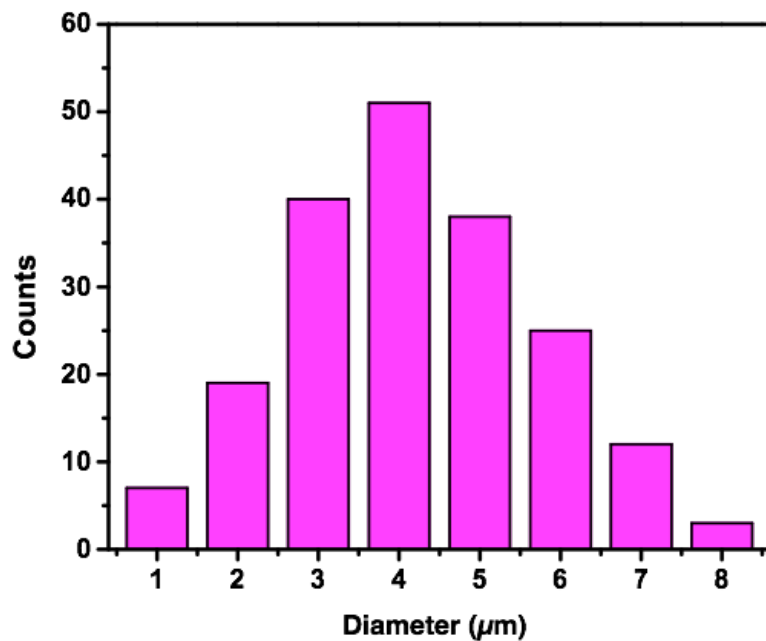


Fig. S2. Size distribution statistics for 2D (C₄H₉NH₃)₂PbBr₄ synthesized using a ternary co-solvent on Si/SiO₂ substrate.

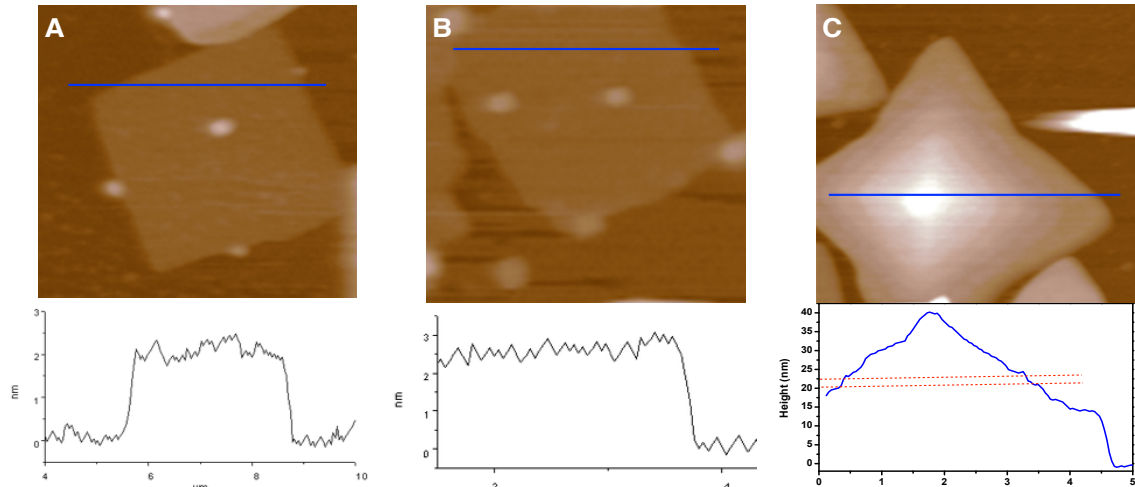


Fig. S3. AFM images of 2D sheets. (A, B) Single layers. (C) A pyramids. It was found some of the sheets with over 30 nm thick show such pyramidal structure. The formation of pyramids may provide important information on the growth mechanism and crystal structures of the 2D hybrid perovskite sheets. Since no spiral is observed, the growth mechanism probably occurs in a layer-by-layer fashion. The formation of the pyramids indicates that there is probably lattice strain between each layer and the new layer stops growth after reaching a certain size. Only a small portion of the thick samples have a pyramidal shape. The majority of sheets are flat, indicating that there may be two growth mechanisms.

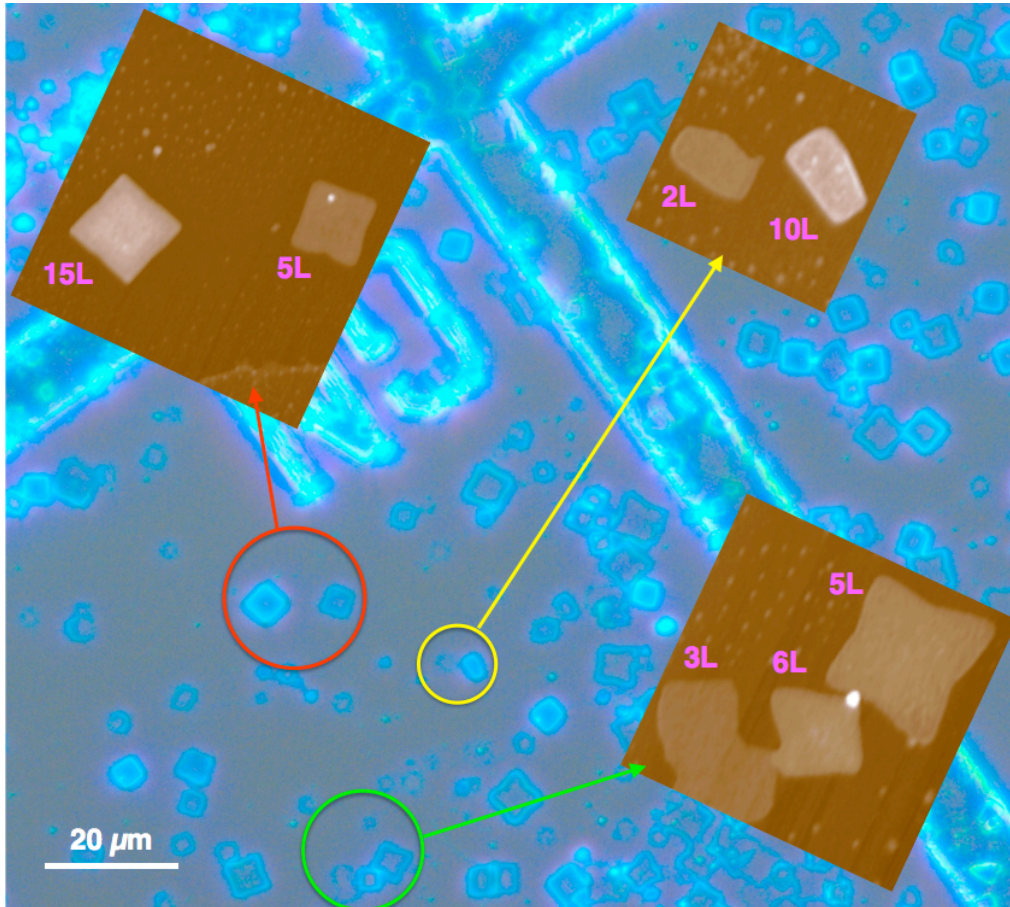


Fig. S4. Correlation between optical image and AFM images for the same 2D sheets. The thin sheets were grown on a labeled SiO_2 substrate (300 nm thermal oxide on Si). Dark field optical images were taken, and then the same spots were measured by AFM. The thinnest sheets that can be seen directly by the optical microscope are double layers.

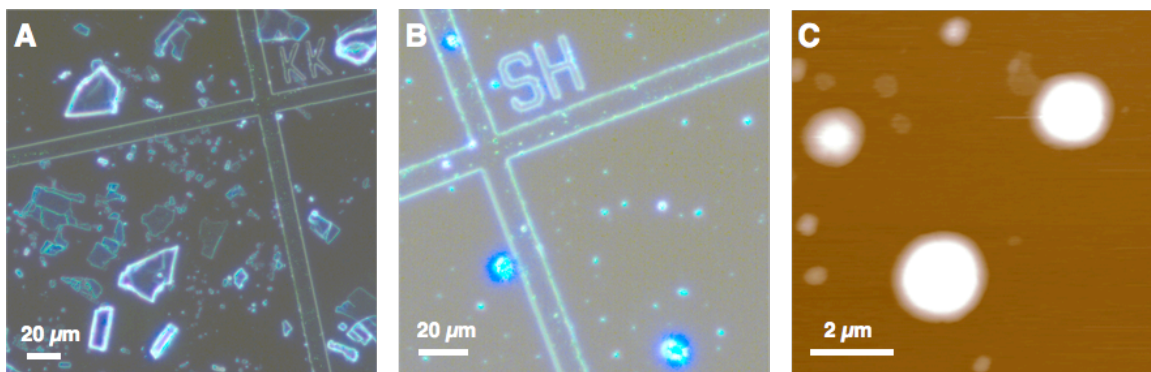


Fig. S5. Exfoliation from large single crystals. (A) Optical image of $(\text{C}_4\text{H}_9\text{NH}_3)_2\text{PbBr}_4$ exfoliated using a scotch tape. The size and thickness of the sheets have very large distribution. (B) Optical image of $(\text{C}_4\text{H}_9\text{NH}_3)_2\text{PbBr}_4$ exfoliated by ultrasonication of the single crystal in hexanes. (C) AFM images of the exfoliated sheets. It is very hard to find a large single layer. The bigger sheets are typically more than 100 nm thick. This is probably because the mechanical properties are not strong enough and the large thin sheets just break into small pieces (less than 200 nm wide).

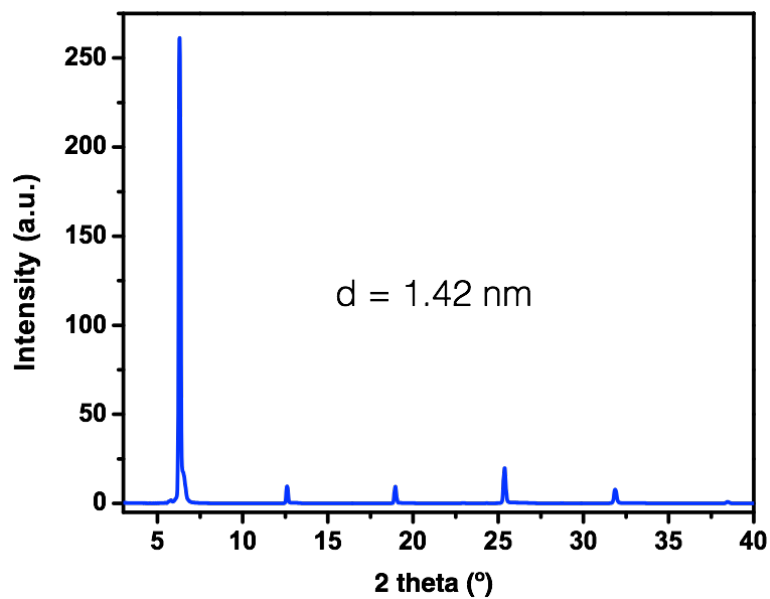


Fig. S6. X-ray diffraction of the solution-grown (C₄H₉NH₃)₂PbBr₄. A relatively more concentrated solution was used to grow highly dense sheets on the substrate to get enough signals for the measurement.

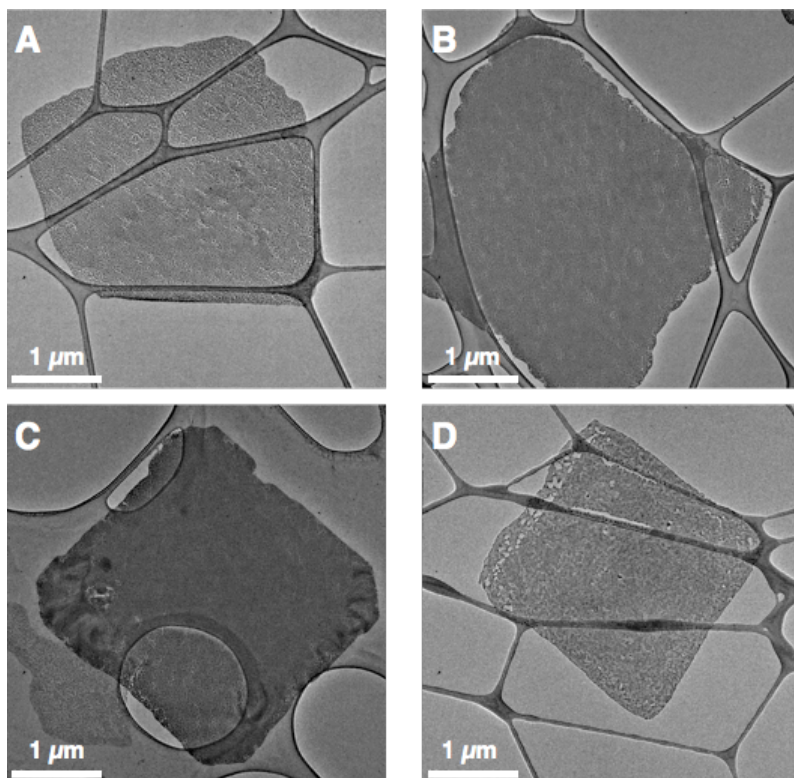


Fig. S7. More examples of the 2D sheets found in the TEM measurements. They all have similar size and shape.

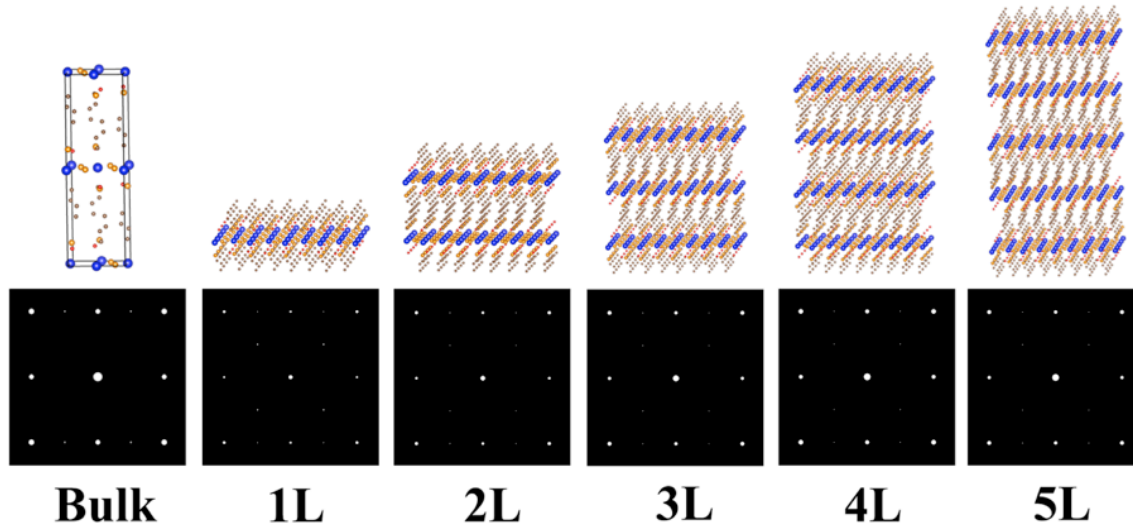


Fig. S8. Simulation of electron diffraction of bulk and 2D sheets with different thicknesses (from 1 layer to 5 layers). Upper row shows the structure models. For bulk ($\text{C}_4\text{H}_9\text{NH}_3$)₂PbBr₄, the unit cell was shown. For 2D sheets with different layers, $4 \times 4 \times 1$ supercells were shown. Lower row shows the corresponding simulated electron diffraction patterns. All the structures exhibit strong (200) and (020) diffraction spots, while their intensities vary. The intensities of the main spots ((200) and (020)) increase as the layer thicknesses increase from 1 layer to 5 layers, and the bulk has the strongest intensity. Looking into details of the minor spots, the bulk shows much stronger (210) diffraction spots (also see Fig. S9) than the 2D thin sheets. Different from the other well-known 2D materials, e.g. graphene, there is not any special stacking sequence among layers (e.g. AB..., ABC...). Therefore, the commonly used method to judge the layer thickness via the intensity ratio of two main spots fails here. Instead, we consider the feature of the (210) spot to be the criterion for roughly judging the thickness. Comparing with the bulk materials, the few-layer 2D sheets exhibit very weak (210) spots. Besides, the weak (110) spots appear in the few-layer 2D sheets. However, the weak spots may not be observed experimentally due to the rapid radiation damage, and only the stronger (200) and (020) main points are maintained (see Fig. S9).

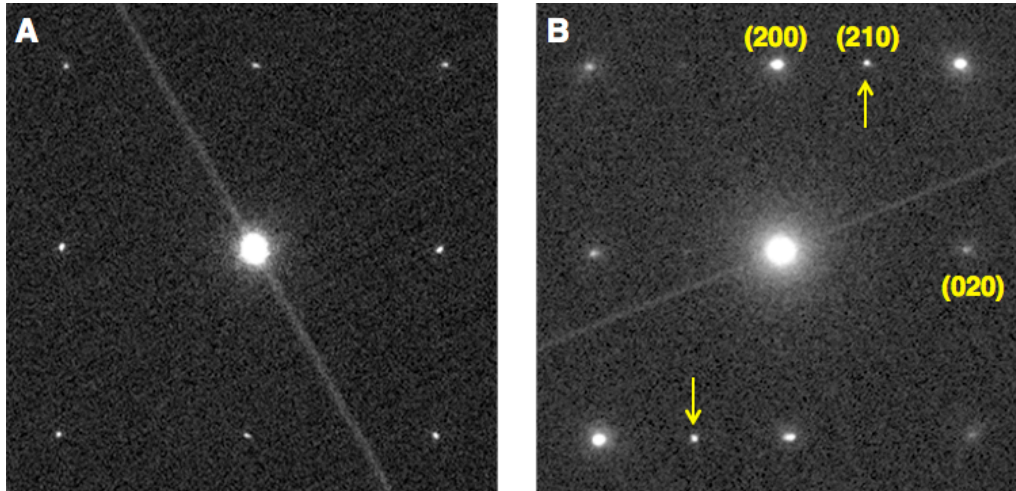


Fig. S9. Experimental electron diffraction patterns of thin-layer (A) and thick-layer (B) 2D sheets. In Fig. S9A, only (200) and (020) main spots can be observed, while apart from stronger main spots, there are also (210) spots in Fig. S9B as indicated by arrows. The diffraction pattern of Fig. S9B was acquired on a sheet with darker contrast in TEM, which was assumed to be thicker than that of Fig. S9A. The asymmetry of the intensity in Fig. S9B was attributed to the rolling-up of the sheet during the electron beam exposure, so that the sheet deviated from the zone axis. Hence, the experimental data supports the above simulation prediction (Fig. S8), that is, thin-layer sheet exhibit only (200) and (020) strong spots, while a thick-layer sheet is bulk-like and shows relatively stronger (210) spots. One point worth mentioning is that sometimes we indeed observe the very weak (210) spots in thin-layer sheets when we take a first look at the diffraction pattern. However, they disappeared so quickly because of the rapid radiation damage, which prevented them to be acquired by the camera even with very short exposure time. The (200) and (020) main spots may even only be visible for a few seconds.

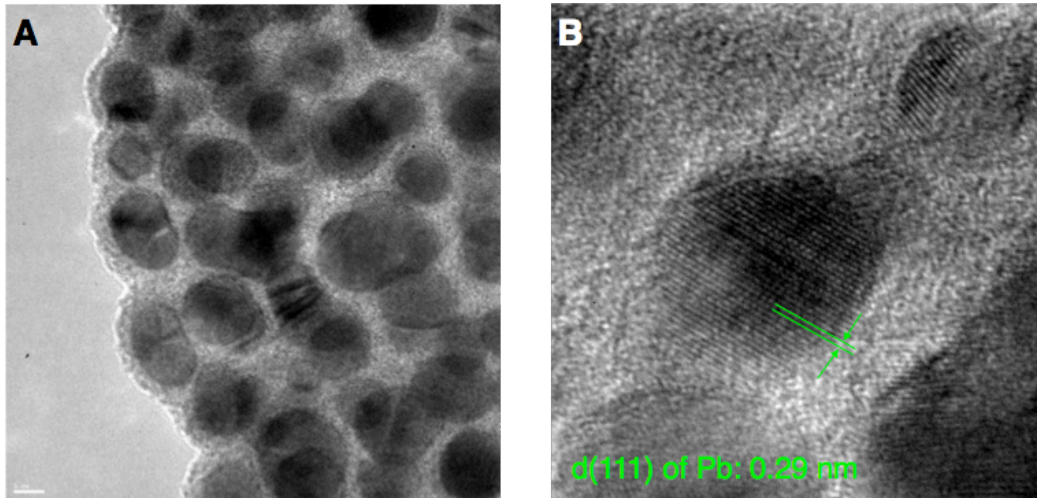


Fig. S10. HRTEM images of the 2D sheets. The sheet has already been damaged when magnification increases so that we cannot obtain an image of the perovskite lattice. Instead, we can observe lots of precipitates of Pb particles (Fig.S10A). A higher magnification in Fig.S10B shows the lattice image of one of the particles. The interplane distance was measured to be 0.29 nm, which agrees with the Pb (111) lattice distance and further confirms the presence of Pb precipitates.

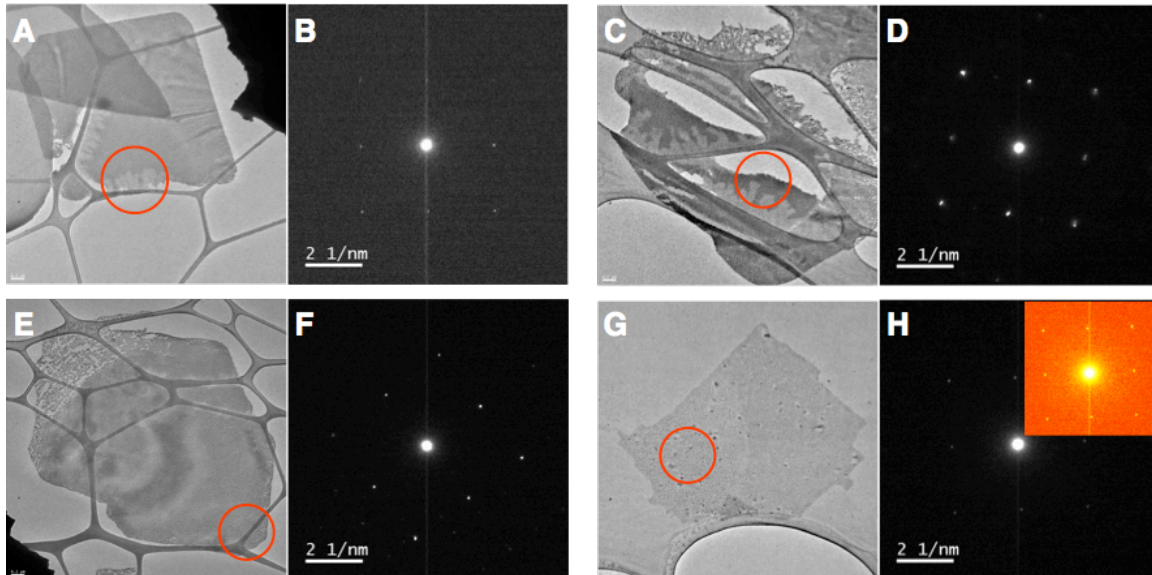


Fig. S11. More examples of the SAED patterns and their corresponding TEM images. The red circles indicate the selected area for diffraction. All the illumination conditions and exposure times were kept the same so that the thicker sheets may have stronger diffraction intensity (D and F), while that of the thinner sheets is weaker (B and H). For H, the intensity becomes too weak to be visible (inset shows the enhanced contrast with false color) and the corresponding sheet is assumed to be very thin. It is challenging to acquire SAED patterns in view of the rapid radiation damage. The method used here is to set the experimental diffraction conditions in advance, and then we move the sample randomly in diffraction mode. We quickly acquired the SAED pattern once it was visible. Then we came back to the image mode with low dose, and gradually increased the dose rate to obtain a suitable contrast for TEM image acquisition. Sometimes the sheets break or roll up as we took images during image acquisition (e.g. A and C).

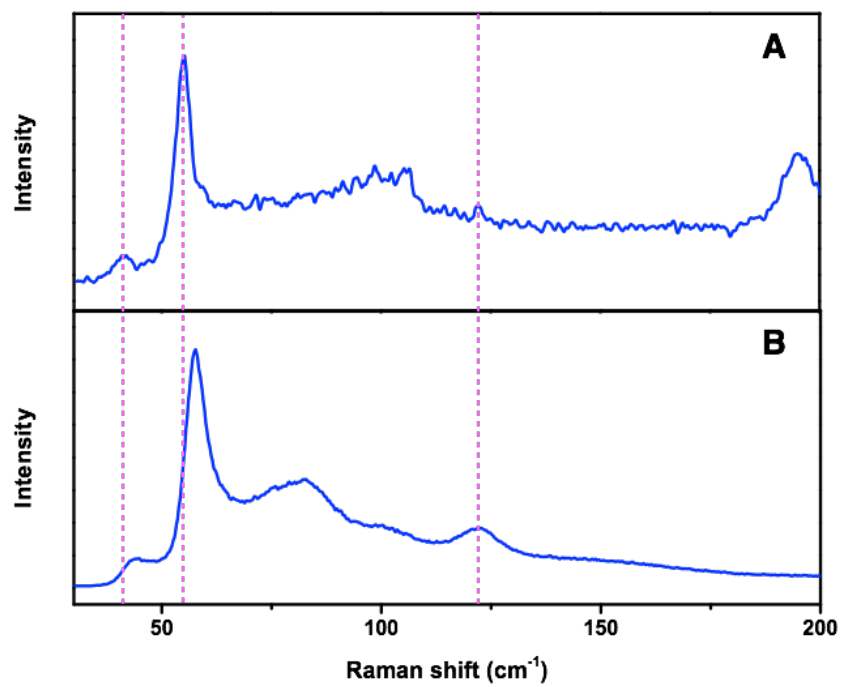


Fig. S12. Raman spectra of the 2D thin sheet and bulk crystal. (A) 2D sheet. (B) Bulk crystal. The signal at ~ 100 and 190 cm^{-1} in (A) are from substrate (Mica).

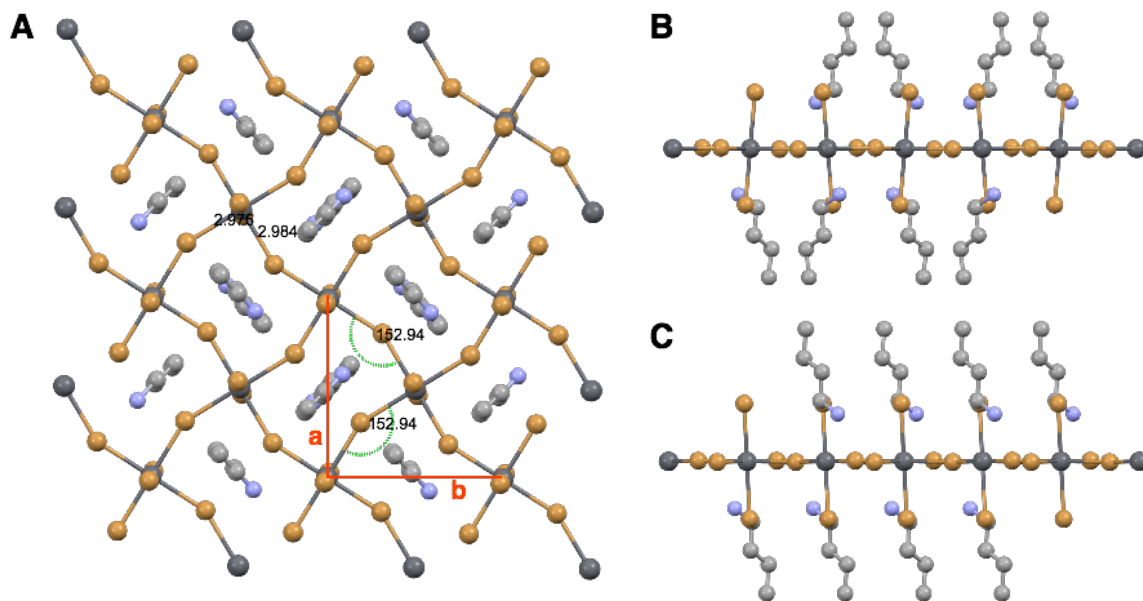


Fig. S13. Single crystal X-ray structure of bulk $(\text{C}_4\text{H}_9\text{NH}_3)_2\text{PbBr}_4$. (A) View from c axis. (B) View from b axis. (C) View from a axis. The Pb-Br-Pb bond angle is 152.94° , which indicates a strong distortion in the a - b plane. For clarity, all hydrogen atoms were removed. Yellow balls, bromine atoms; black balls, lead atoms; grey balls, carbon atoms; blue balls, nitrogen atoms.

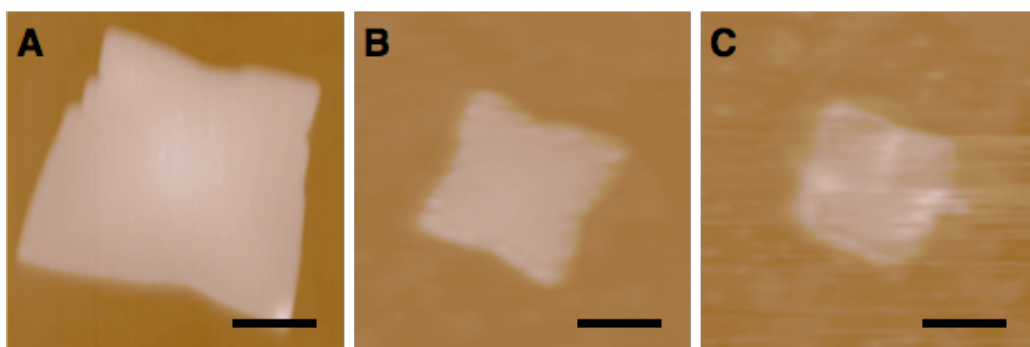


Fig. S14. AFM images of the $(\text{C}_4\text{H}_9\text{NH}_3)_2\text{PbBr}_4$ sheets with 22 layers (A), 8 layers (B), and 3 layers (C).

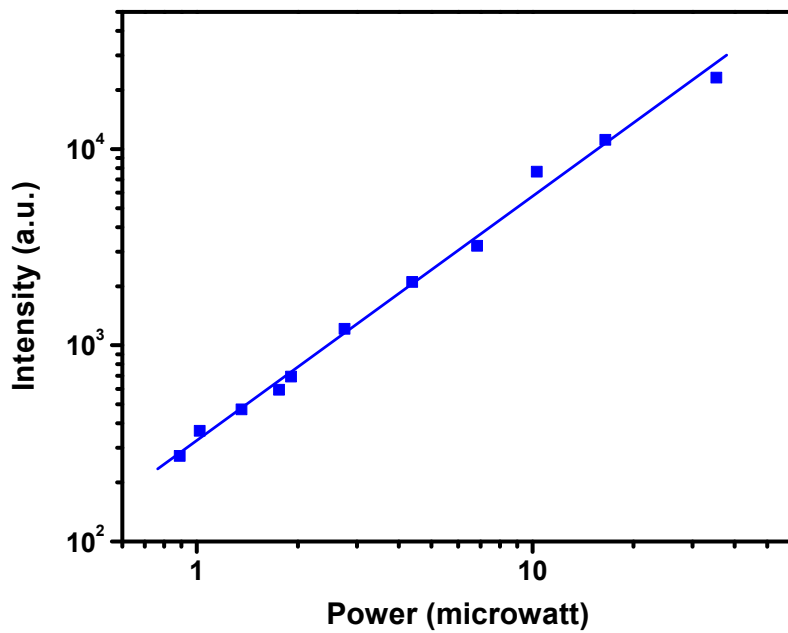


Fig. S15. Excitation power dependence of the photoluminescence as measured at room temperature.

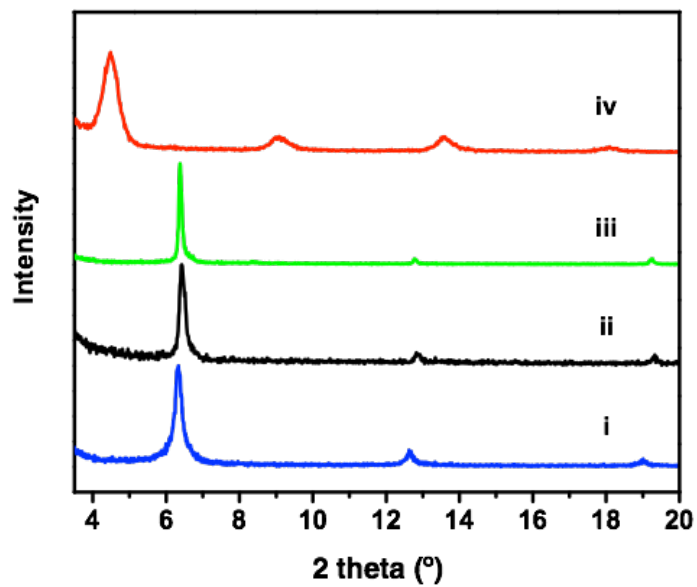


Fig. S16. X-ray diffraction spectra of $(\text{C}_4\text{H}_9\text{NH}_3)_2\text{PbCl}_4$ (i), $(\text{C}_4\text{H}_9\text{NH}_3)_2\text{PbBr}_4$ (ii), $(\text{C}_4\text{H}_9\text{NH}_3)_2\text{PbI}_4$ (iii), and $(\text{C}_4\text{H}_9\text{NH}_3)_2(\text{CH}_3\text{NH}_3)\text{Pb}_2\text{Br}_7$ (iv) 2D sheets.

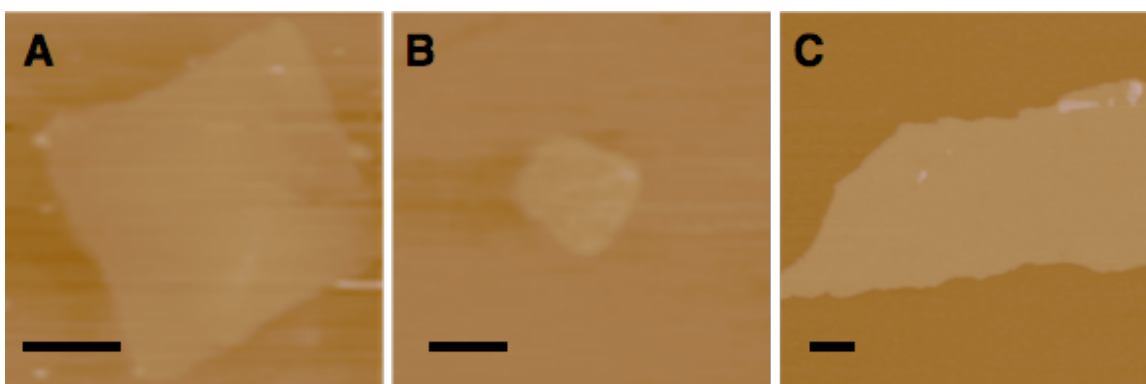


Fig. S17. AFM images of $(\text{C}_4\text{H}_9\text{NH}_3)_2\text{PbCl}_4$ (A), $(\text{C}_4\text{H}_9\text{NH}_3)_2\text{PbI}_4$ (B), and $(\text{C}_4\text{H}_9\text{NH}_3)_2(\text{CH}_3\text{NH}_3)\text{Pb}_2\text{Br}_7$ (C) 2D sheets with 5, 2, and 4 layers thick; respectively. Scale bars are 2 μm .

Supplementary tables

Table S1. Single crystal X-ray diffraction data of $(C_4H_9NH_3)_2PbBr_4$.

Empirical formula	C ₈ H ₂₄ Br ₄ N ₂ Pb	
Formula weight	675.12	
Temperature	100(2) K	
Wavelength	0.71073 Å	
Crystal system	Orthorhombic	
Space group	P b c a	
Unit cell dimensions	a = 8.2530(2) Å	a = 90°.
	b = 8.1375(2) Å	b = 90°.
	c = 27.4028(9) Å	g = 90°.
Volume	1840.34(9) Å ³	
Z	4	
Density (calculated)	2.437 Mg/m ³	
Absorption coefficient	17.833 mm ⁻¹	
F(000)	1232	
Crystal size	0.040 x 0.040 x 0.020 mm ³	
Theta range for data collection	1.486 to 25.355°.	
Index ranges	-9<=h<=9, -9<=k<=9, -33<=l<=33	
Reflections collected	28141	
Independent reflections	1678 [R(int) = 0.0376]	
Completeness to theta = 25.000°	100.0 %	
Absorption correction	Semi-empirical from equivalents	
Max. and min. transmission	0.745 and 0.428	
Refinement method	Full-matrix least-squares on F ²	
Data / restraints / parameters	1678 / 0 / 72	
Goodness-of-fit on F ²	1.279	
Final R indices [I>2sigma(I)]	R1 = 0.0225, wR2 = 0.0440	
R indices (all data)	R1 = 0.0269, wR2 = 0.0452	
Extinction coefficient	n/a	
Largest diff. peak and hole	0.953 and -0.761 e.Å ⁻³	

Table S2. Atomic coordinates ($\times 10^4$) and equivalent isotropic displacement parameters ($\text{\AA}^2 \times 10^3$) of $(\text{C}_4\text{H}_9\text{NH}_3)_2\text{PbBr}_4$.

	x	y	z	U(eq)
C(1)	4572(6)	5329(6)	8853(2)	20(1)
C(2)	4765(6)	5236(6)	8307(2)	16(1)
C(3)	3620(7)	6372(7)	8040(2)	26(1)
C(4)	3800(8)	6253(8)	7489(2)	39(2)
N(1)	5751(5)	4222(5)	9103(2)	14(1)
Br(1)	4692(1)	5176(1)	6095(1)	14(1)
Br(2)	6904(1)	8106(1)	5013(1)	14(1)
Pb(1)	5000	5000	5000	9(1)

Table S3. Bond lengths [\AA] and angles [$^\circ$] for $(\text{C}_4\text{H}_9\text{NH}_3)_2\text{PbBr}_4$.

C(1)-N(1)	1.493(6)
C(1)-C(2)	1.506(7)
C(1)-H(1A)	0.9900
C(1)-H(1B)	0.9900
C(2)-C(3)	1.512(6)
C(2)-H(2A)	0.9900
C(2)-H(2B)	0.9900
C(3)-C(4)	1.519(8)
C(3)-H(3A)	0.9900
C(3)-H(3B)	0.9900
C(4)-H(4A)	0.9800
C(4)-H(4B)	0.9800
C(4)-H(4C)	0.9800
N(1)-H(1C)	0.9100
N(1)-H(1D)	0.9100
N(1)-H(1E)	0.9100
Br(1)-Pb(1)	3.0138(5)
Br(2)-Pb(1)	2.9762(4)
Br(2)-Pb(1)#1	2.9843(4)
Pb(1)-Br(2)#2	2.9762(4)
Pb(1)-Br(2)#3	2.9843(4)
Pb(1)-Br(2)#4	2.9843(4)
Pb(1)-Br(1)#2	3.0138(5)

N(1)-C(1)-C(2)	111.1(4)
N(1)-C(1)-H(1A)	109.4
C(2)-C(1)-H(1A)	109.4
N(1)-C(1)-H(1B)	109.4
C(2)-C(1)-H(1B)	109.4
H(1A)-C(1)-H(1B)	108.0
C(1)-C(2)-C(3)	112.6(4)
C(1)-C(2)-H(2A)	109.1
C(3)-C(2)-H(2A)	109.1
C(1)-C(2)-H(2B)	109.1
C(3)-C(2)-H(2B)	109.1
H(2A)-C(2)-H(2B)	107.8
C(2)-C(3)-C(4)	112.4(5)
C(2)-C(3)-H(3A)	109.1
C(4)-C(3)-H(3A)	109.1
C(2)-C(3)-H(3B)	109.1
C(4)-C(3)-H(3B)	109.1
H(3A)-C(3)-H(3B)	107.8
C(3)-C(4)-H(4A)	109.5
C(3)-C(4)-H(4B)	109.5
H(4A)-C(4)-H(4B)	109.5
C(3)-C(4)-H(4C)	109.5
H(4A)-C(4)-H(4C)	109.5
H(4B)-C(4)-H(4C)	109.5
C(1)-N(1)-H(1C)	109.5
C(1)-N(1)-H(1D)	109.5

H(1C)-N(1)-H(1D)	109.5
C(1)-N(1)-H(1E)	109.5
H(1C)-N(1)-H(1E)	109.5
H(1D)-N(1)-H(1E)	109.5
Pb(1)-Br(2)-Pb(1)#1	152.940(17)
Br(2)-Pb(1)-Br(2)#2	180.0
Br(2)-Pb(1)-Br(2)#3	89.222(4)
Br(2)#2-Pb(1)-Br(2)#3	90.778(4)
Br(2)-Pb(1)-Br(2)#4	90.778(4)
Br(2)#2-Pb(1)-Br(2)#4	89.222(4)
Br(2)#3-Pb(1)-Br(2)#4	180.0
Br(2)-Pb(1)-Br(1)	89.573(12)
Br(2)#2-Pb(1)-Br(1)	90.429(12)
Br(2)#3-Pb(1)-Br(1)	94.874(12)
Br(2)#4-Pb(1)-Br(1)	85.126(12)
Br(2)-Pb(1)-Br(1)#2	90.427(12)
Br(2)#2-Pb(1)-Br(1)#2	89.571(12)
Br(2)#3-Pb(1)-Br(1)#2	85.125(12)
Br(2)#4-Pb(1)-Br(1)#2	94.875(12)
Br(1)-Pb(1)-Br(1)#2	180.000(15)

Symmetry transformations used to generate equivalent atoms:
#1 $x+1/2, -y+3/2, -z+1$ #2 $-x+1, -y+1, -z+1$ #3 $-x+3/2, y-1/2, z$
#4 $x-1/2, -y+3/2, -z+1$

Table S4. Anisotropic displacement parameters ($\text{\AA}^2 \times 10^3$) for $(\text{C}_4\text{H}_9\text{NH}_3)_2\text{PbBr}_4$. The anisotropic displacement factor exponent takes the form: $-2\pi^2 [h^2 a^{*2} U^{11} + \dots + 2 h k a^* b^* U^{12}]$.

	U^{11}	U^{22}	U^{33}	U^{23}	U^{13}	U^{12}
C(1)	21(2)	24(2)	12(3)	1(2)	1(2)	2(2)
C(2)	19(2)	15(2)	14(3)	1(2)	0(2)	6(2)
C(3)	25(3)	33(3)	21(3)	7(2)	-5(2)	-2(2)
C(4)	35(3)	62(4)	21(3)	13(3)	-5(3)	-3(3)
N(1)	16(2)	15(2)	12(2)	0(2)	3(2)	-1(2)
Br(1)	16(1)	14(1)	12(1)	1(1)	-2(1)	2(1)
Br(2)	13(1)	12(1)	17(1)	-1(1)	2(1)	-4(1)
Pb(1)	9(1)	8(1)	10(1)	0(1)	0(1)	0(1)